IEEE Transactions on Field Robotics (T-FR) paper, presented at ICRA 2026, Vienna, Austria. Cite as T-FR paper.
IEEE Transactions on Field Robotics
Special Issue on Space Robotics

Received 21 February 2025; revised 19 July 2025 and 27 September 2025; accepted 11 November 2025.
Date of publication 14 November 2025; date of current version 3 December 2025.
This article was recommended by Executive Editor David Wettergreen.

Digital Object Identifier 10.1109/TFR.2025.3633215

Novel Robotic Fleet for Sample Recovery in Lunar Craters: A Concept of Operations

R. JANGALE (Graduate Student Member, IEEE), D. PRAVECEK (Graduate Student Member, IEEE), S. LAM, D. MCDOUGALL, M. TREVIÑO IV, A. VILLANUEVA (Member, IEEE), J. LAND, H. DE LEON, M. OEVERMANN (Member, IEEE), AND R. AMBROSE (Member, IEEE)

Robotics and Automation Design (RAD) Laboratory, Texas A&M University, Bryan, TX 77807 USA

CORRESPONDING AUTHOR: R. JANGALE (rishijangale@tamu.edu)

This work was supported in part by the Texas Governor's University Research Initiative (GURI) and in part by the Texas A&M Chancellor's Research Initiative (CRI).

(Regular Article)

ABSTRACT Exploration of extraterrestrial surfaces, such as the lunar surface, can prove treacherous for humans and robots alike and requires highly specialized mobility platforms to ensure the success of a mission and the safety of any operators. However, these specialized machines may limit the overall scope of a mission by limiting the performance outside a particular environment. Thus, for maximum capabilities, a team of distinct but complementary specialized robots and vehicles may be used to expand mission capabilities in lunar environments. In this article, a concept of operations for exploration of a lunar crater from utilizing a collaboration between a wheeled rover, represented by the Robotics and Automation Design (RAD) Laboratory exploration vehicle (REV) and a nontraditional spherical robot, represented by RoboBall II, is introduced. These robots are used as an analog for mission-capable robots such as NASA's Chariot rover and the larger RoboBall III. Design of these robots, along with collaborative features and intended operational environments, is discussed. A controller for RoboBall to attempt controlled descent on slopes is presented. Furthermore, a ballistic sample return module for collection and ex situ analysis of a sample from the bottom of a lunar crater, along with potential navigational mechanisms to facilitate efficient recovery, is presented. Finally, a mission analog using RoboBall III and the ballistic sample return conducted in a former quarry is demonstrated.

INDEX TERMS Extraterrestrial mobility, lunar crater exploration, mission design, multirobot collaboration, sample acquisition and return, spherical robots, wheeled rovers.

I. INTRODUCTION

HUMANITY has returned its focus to the moon. In tandem with private sector interest, the launch of United States' Artemis, India's Chandrayaan, South Korea's Danuri, and China's Chang'e programs has increased interest in lunar landing, mobility, measurement, and sample return capability. While this may not be humanity's first time there, the moon still provides challenging environments for exploration for astronauts and rovers alike. It is clear that efficient interaction between unique robots, especially the cooperation of robots catered to different tasks, will prove invaluable to the safety and success of lunar exploration missions.

Collaboration between teams of specialized robots for extraterrestrial exploration has been considered. Aoki et al. [1] proposed a parent–child rover system with their Tri-Star IV rover, enabling the descent of a child rover into craters using a tether. This allowed a rover to descend into the permanently shadowed region of a crater and return with a sample. However, the range of the child rover is severely limited by the length of the tether. Kingry et al. [2] discuss a control scheme for a system consisting of a mobile solar charging station robot with multiple smaller worker robots, allowing for the extended operational range of the worker robots. Schenker et al. [3] described a system of rovers for

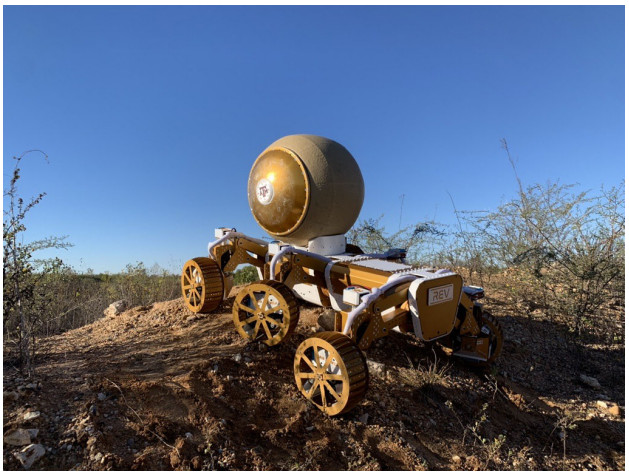

FIGURE 1. **Multirobot collaboration between REV rover and RoboBall II approaching a mock crater edge.**

Martian sample collection and analysis. A lander equipped with science equipment can deploy a sample return rover that can retrieve a sample for the lander, allowing for the rover to remain lightweight while sensitive scientific equipment remains stationary aboard the lander. Furthermore, the lander may contain another robot in the form of a Mars Ascent Vehicle. This integrated system allows for an extraterrestrial sample's acquisition, processing, and return through specialized multirobot collaboration.

At a more general, higher level, most rover spacecraft, such as the Mars Science Laboratory, can be considered such teams, involving the spacecraft itself, the lander, and the onboard rover payload [4]. Each of the unique vehicles complementarily increases the overall mission capabilities. On an orbital scale, NASA's proposed Gateway architecture integrates sample return rovers, landers, and ascent vehicles with space stations in orbit, enhancing the transfer of data, samples, and astronauts between the Moon, Earth, and beyond [5]. There is value in the design of space missions that exploit the strengths of diverse, specialized robotic teams while mitigating the weaknesses of individual members.

Design of specialized mobile robots to tackle the complex and treacherous terrains of extraterrestrial environments requires consideration of every component of the individual members of the extraterrestrial robotic team. A classic member of such a team is the wheeled rover. Substantial work has been done to attempt to better suit wheeled rovers for terrain-robust mobility, where slopes in particular are a feature that requires careful consideration in design and mobility techniques. Kim et al. [6] discussed an optimal design methodology for rover wheels using constraints such as axial load, slip ratio, and velocity in a given operational environment. Nakashima et al. [7] performed finite element analysis on a single lunar rover wheel to characterize the rover's performance on slopes and determine if the wheel design had to be changed to tackle steeper grades. Wheel design was combined with an articulated body in [8], where they experimented with decreasing slippage using active control of the rover body composed of a 3-DOF articulated frame. Similarly, Zhang et al. [9] used a passive suspension system to increase the rover's ability to handle unstable terrain while minimizing rover bouncing and modeled the maneuverability and stability of a crewed rover. The Spirit and Opportunity rovers used a rocker-bogie passive suspension, allowing the rover to traverse over obstacles 25 cm on a maximum slope of 20° [10].

Active suspension further extends the maneuverability of rovers by allowing greater adaptation through actively actuated configurations that can combine the advantages of wheeled and legged rovers. This also allows rovers to use unique locomotion techniques to attempt to independently unstick themselves. NASA's VIPER rover planned to use a crawling and digging motion to become unstuck [11], while the Sherpa rover used its legs as leverage for negative ground clearance traversal [12]. Along with these improvements in hardware, novel traversal techniques augmenting or replacing wheeled rovers were developed, such as the Icebreaker rover described in [13], which uses a combination of tracks and a plowing instrument to increase mobility on slopes.

Many of these technologies were combined at the Johnson Space Center (JSC) in the Chariot rover, which was designed to resolve limitations in NASA's Lunar Roving Vehicle using improvements in mobility technology [14]. This rover's six independent 3-DOF wheel modules gave it exceptional mobility and robustness while traveling over rough terrain. While improvements in these wheeled rovers have increased maneuverability, traversability, and stability over most terrains, these rovers still risk becoming stuck or flipped on steep slopes, and are limited to slow rates of descent to ensure stability [15]. Collaboration between these more general terrain rovers and a rover suited to crater descent will extend the operational efficiency and robustness of the mission's actors.

In contrast to wheeled rovers, spherical robots eliminate this vulnerability by reimagining the rover as a self-contained system within a pressurized, spherical shell, rather than relying on external wheels. This innovative design not only negates the concept of "up" or "down," making tip-overs impossible but also provides exceptional resilience against environmental hazards such as sand, dust, and liquid, as the sealed spherical shell acts as a protective shield. Unlike traditional rovers, whose descending capabilities are constrained by actuator torque limits, the slope performance of the pendulum-driven spherical robots is governed by the ratio of its radius to the center of gravity of its internal pendulum [16]. By virtue of having an internal pendulum, spherical robots are often isolated from their environment and have limited payload capabilities, whereas wheeled rovers can carry much larger payloads [14]. Furthermore, while spherical robots are well suited to slope descent due to their geometry and drive mechanisms, their slope ascent capabilities are limited, as explored by Jangale et al. [16]. As such, a spherical robot

is not suited for general transit and exploration on the lunar surface, incentivizing cooperation with a robot, such as a wheeled rover, that is more suited for these terrains. Such a rover could effectively transport a spherical robot, as shown in Fig. 1, to a desired mission site while maintaining its generality.

This article proposes a cooperative multirobot team consisting of wheeled and spherical rovers for sample collection from lunar craters. Section II will describe RoboBall II, RoboBall III, and the Robotics and Automation Design (RAD) Laboratory exploration vehicle (REV) robots used for testing by the RAD Laboratory and their real-world mission counterparts, while Section III will describe their modes of operation and capabilities and proposed interactive features between the robots. The RoboBalls' control algorithm to attempt a controlled slope descent can be found in Section IV. Section V will describe the ballistic sample return module to be added to RoboBall III, allowing for long-range return of a sample from within a crater, along with a description of potential sample location and recovery methods in Section VI. Finally, previously discussed innovations will be combined in a comprehensive mission plan for operation in a lunar environment in Section VII, along with preliminary results in an analog mission test conducted on similar terrestrial terrain.

II. BACKGROUND

The RAD Laboratory was founded at Texas A&M University in 2022 to create next-generation robotic mobility systems for Earth's and space environments. Inspired by the VIPER and Martian sample return programs, the RAD Laboratory has developed a promising new approach to recovering samples from the depths of lunar craters. The first of these systems is the RoboBall program, which has developed a series of inflatable pendulum-driven spherical robots designed for chaotic or controlled descent into a crater. The smaller, 0.61 m (2 ft) diameter RoboBall II was first built as a proof of concept and controls test bed to validate the RoboBall concept [15]. As the first soft robot of its kind, this prototype allowed for initial dynamics and control studies to better study control strategies for this unique system [17]. While RoboBall II can be outfitted with sensors for reconnaissance and surveillance, its lack of a cargo bay limits it to an observational interaction with its environment. Work done on RoboBall II has translated into its larger, 1.8 m (6 ft) diameter counterpart, RoboBall III. To add the ability to interact with its environment, RoboBall III was designed with an annular payload bay region in its driveshaft [16]. This system would allow for an inflatable, scalable system to carry payloads and scientific instruments to areas of interest in record time, ideally down the sloped walls of a crater such as the Shackleton crater at the lunar south pole.

The RAD Laboratory has branched from JSC's work on the previously mentioned Chariot by constructing REV, a smaller prototype rover with similar active suspension characteristics. Although slower and less robust at descending slopes than RoboBall, REV is a multipurpose, general-terrain vehicle that delivers RoboBall to its mission zone to explore terrains where wheeled rovers may struggle. REV and RoboBall II will serve as an analog for JSC's Chariot and RoboBall III, respectively, allowing for the development of mission schemes at a manageable scale while still enabling field testing of the RoboBall III system. By using the smaller analogs of the mission-capable robots, software, control algorithms, and the interaction between them can be tested and iterated on a safer and faster scale. These robots can be seen in Fig. 2.

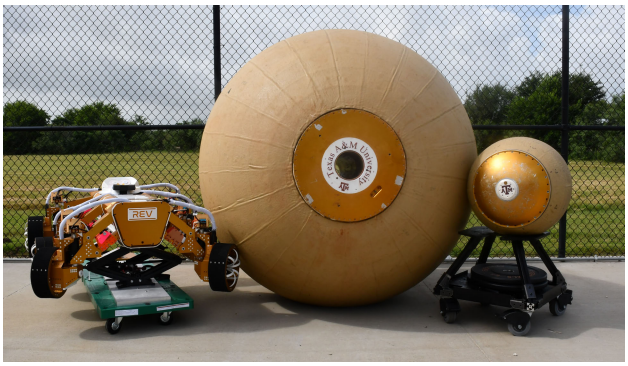

FIGURE 2. **Proposed crater descent and exploration robotic fleet: RoboBall II (right) and its mission-capable counterpart, RoboBall III (middle). The REV (left), a small-scale analog to NASA JSC's Chariot (not shown) [18].**

Exploring the necessary components for a complementary spherical robot-rover lunar exploration ecosystem, such as integrated transport, controlled slope descent, and sample return/recovery, combined into a novel mission concept, is the primary contribution of this article.

A. MISSION CONCEPT

This combination of robots will be able to approach a crater, deploy RoboBall to descend rapidly, collect and return a sample to outside the crater, and retrieve the returned sample for further analysis. Throughout this article, design requirements deemed important for such a mission will be discussed, along with a conducted analog mission in a terrestrial crater. The contribution of each of the previously mentioned components to overall mission success will be discussed in individual sections, with a detailed mission plan for each component to be presented in Section VII.

This mission will offer several advantages over existing lunar crater exploration missions, the most significant of which is the substantially increased range. Compared with tether-based crater missions, such as Tri-Star IV, DuAxel, or the Moon-Diver concept, the range of this mission is far larger as it is not limited to a physical connection outside the crater, but is rather limited by the battery capacity of RoboBall. This mission allows for the return of samples from deeper within craters of interest, while enabling rapid, robust descent. Furthermore, this combination of rover and spherical robots does not require the mission to be planned entirely around crater descent, but rather allows a general-purpose

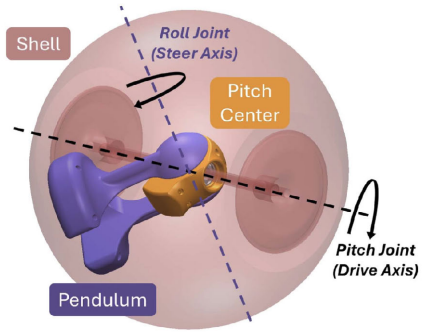

FIGURE 3. **RoboBall's links and joints labeled in a kinematic model.**

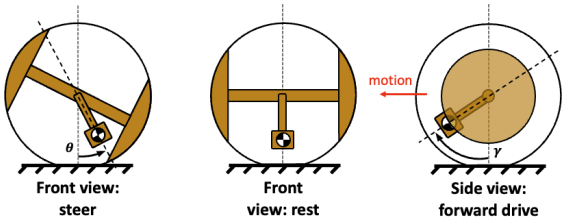

FIGURE 4. **RoboBalls' locomotive mechanisms shown in isolation.**

wheeled rover to deliver RoboBall to a crater without compromising the primary rover, increasing the potential scope of a greater mission outside crater descent.

III. ROBOT OVERVIEWS

A. PENDULUM-DRIVEN SPHERICAL ROBOT DESCRIPTION

The RoboBall platform consists of two main parts: an interior 2-DOF pendulum and an outer soft shell connected via a drive shaft.

Both RoboBalls' shells are constructed from a two-part elastomer [16], [19]. This article has a high tensile strength (approximately 17 MPa, 2.5 ksi) and is designed for high wear resistance, as minimal wear has been observed after significant testing with either robot. This pressurized shell also provides an atmosphere for convective cooling of components onboard the pendulum, as opposed to the radiative heat dissipation that may be required with traditional vehicles. The shell also environmentally isolates critical robot components from dust or regolith. RoboBall II operates at a nominal pressure of 20–35 kPa (3–5 psi) and RoboBall III at a pressure of 10.4–11 kPa (1.5–1.6 psi). These pressures are calculated with the aim of maintaining a minimum ground clearance of the pendulum with the contact patch of the shell [15]. This, coupled with its soft-pressurized nature, allows the robot to absorb impacts more effectively without damaging the pendulum. At their respective operating pressures, RoboBall II has an average leak rate of 0.55 kPa (0.08 psi) per minute, and RoboBall III has a leak rate of 0.028 kPa (0.004 psi) per minute [20]. In lunar environments, this pressure can be expected to be 1/6th of the nominal Earth operating pressure. Furthermore, a higher density inert gas, such as argon, can be used to inflate the shell, reducing the leak-rate compared with air.

In addition to the shell, RoboBall features both pitch center and pendulum links for propulsion and steering. These linkages, along with reference axes, are illustrated in Fig. 3. RoboBall moves forward when the pendulum rotates about the pitch joint/drive axis. When motors in the pitch center spin, the rotation of the pendulum about the pitch joint/drive axis shifts mass forward, causing the shell to rotate forward and RoboBall to propel forward. Notably, this rotation around the pitch joint is continuous, and as such, it allows RoboBall to drive continuously. To steer, the motors in the pendulum rotate the pendulum about the roll joint/steer axis. Similar to the propulsion operation, this shift in mass causes RoboBall to tilt the pendulum about the joint/steer axis, resulting in RoboBall rolling sideways. This operation is not continuous, so the robot is considered non-holonomic. As this mass is shifted, be it in the drive or the steer directions, RoboBall will accelerate in that direction. Isolated pendulum motions and their respective DOFs can be seen from Fig. 4. The symmetry between the drive and steer directions is often exploited while modeling, as shown in [21], [22], and [23].

This pendulum also carries all critical robot components, including actuators, electronics, telemetry, and batteries. Due to the nature of RoboBall as a consumable, short-life robot, batteries prove sufficient as a power supply, and can safely withstand the dynamic motion of the pendulum.

The two current RoboBall models are RoboBall II and RoboBall III. RoboBall II and III, along with their subsystems, can be seen from Figs. 5 and 6, respectively. Notably, RoboBall II has a smaller shell radius and does not have the capability to carry a payload, but it is still suitable for surveying and exploration. RoboBall III, however, has a hollow driveshaft that functions as a payload bay. This, along with other relevant differences, can be seen from Table 1.

B. ROVER DESCRIPTION

While typical wheeled or tracked vehicles are robust, they often have limited mobility in complex terrain. On the other hand, legged robots can step over complex obstacles, but are fragile and have lower load capacities. Facing the challenge of designing a mobility platform that is both robust and high-performing, NASA developed a wheel-leg hybrid system designed to leverage the robustness of typical tracked vehicles and the terrain handling of a legged system. This system has been implemented for a series of rovers, such as Chariot [18], Mini Rover [24], Resource Prospector, and Lunar Terrian Vehicle [25]. Although the number of legs and other geometric parameters may vary, the core kinematics remain the same: independently actuated suspension, steer, and drive. The increased DOFs open up new control

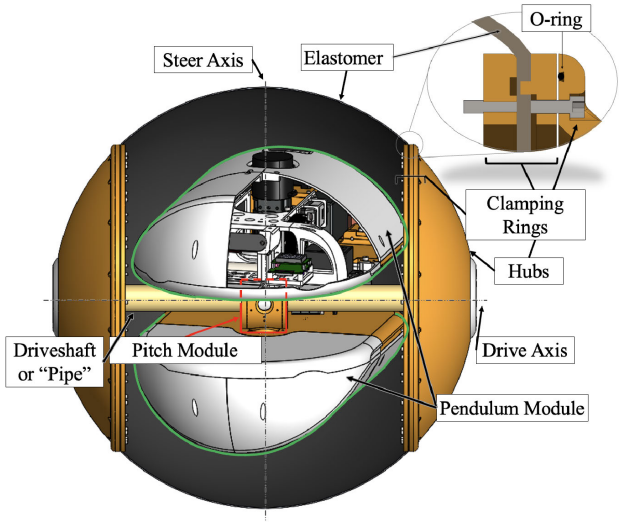

FIGURE 5. **Critical components and subsystems of RoboBall II are shown the pendulum (outlined green) and the pitch module (outlined red).**

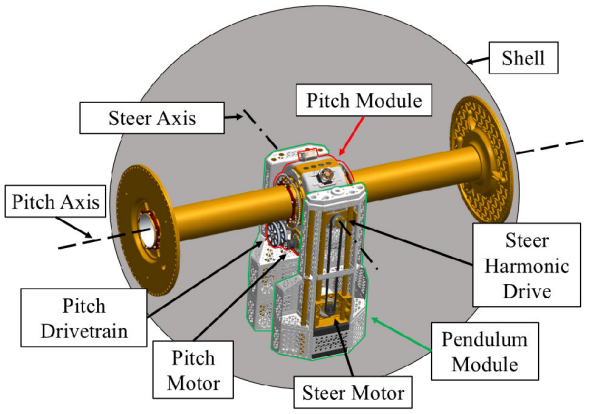

FIGURE 6. **Critical components and subsystems of RoboBall III are shown the pendulum (outlined green) and the pitch module (outlined red).**

opportunities to traverse rugged terrain more effectively. However, the full potential of mobility and capability for this mobile system has not been fully explored. To address this, REV follows the same kinematic structure as the wheel-leg hybrid and aims to serve as a smaller scale control testbed for an extreme mobility rover chassis. This vehicle also serves as a more accessible and manageable counterpart to a full-scale, mission-capable rover such as Chariot. Because REV is a representative testbed, it uses LiFePO4 batteries. However, in real operation, solar or nuclear power sources for Chariot could be considered [18].

Designed using mostly aluminum sheet metal, it consists of six independent and alike leg modules, each having 3-DOF: suspension, steer, and drive, as shown in Fig. 7. Each independent DOF is defined in Fig. 8. REV's key parameters, along with the parameters of its analog Chariot, are summarized in Table 2.

TABLE 1. **RoboBall II and RoboBall III comparison [16].**

Parameter	RII	RIII
Total Mass	39.1 kg	154.0 kg
Shell Radius	0.305 m	0.91 m
Actuator Stall Torque	2.6 Nm	6.08 Nm
Drivetrain Reduction	21:1	21.5:1
Steer Reduction	21:1	50:1
Max Slope Climb	7.89°	9°
Pend. Angle at Max Slope	65.1°	47°
Payload Geometry	None	Cylindrical
Payload Length	N/A	0.86 m
Payload Radius	N/A	0.152 m
Operating Voltage	12 V	48 V
Battery Composition	LiFePO4	AGM
Battery Configuration	2 Parallel	4 Series
Total Capacity	480 Wh @ 12 V	1008 Wh @ 48 V

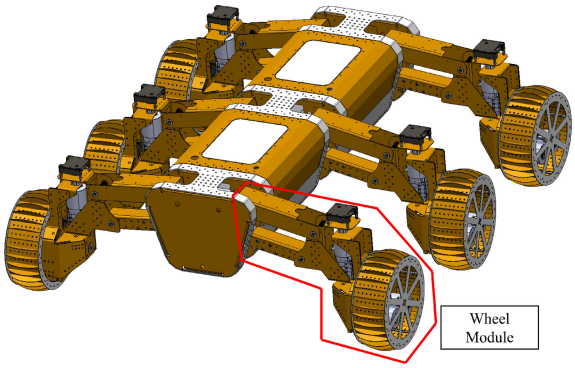

FIGURE 7. **CAD model of the REV rover with a single-wheel module labeled.**

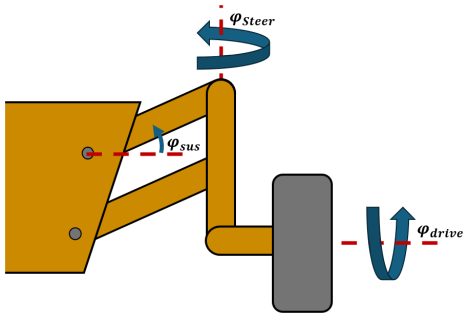

FIGURE 8. **Front view of a single-REV leg module with each of the 3-DOF labeled.**

While all the DOFs generally contribute to higher mobility, the active suspension DOF makes REV uniquely capable

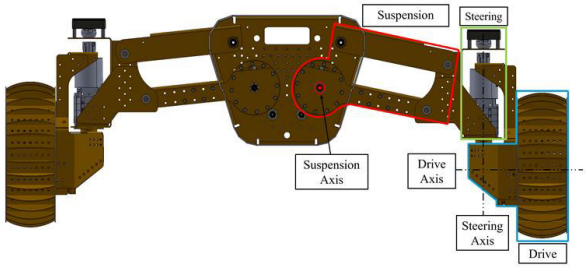

FIGURE 9. Front view of REV with all subsystems and axes defined and labeled.

of balancing difficult-to-capture loads, such as RoboBall. When traversing typically rough terrain, REV can leverage its suspension to articulate the pitch and attitude of its chassis to balance the payload on top of it. The ability to lift individual wheels is beneficial when encountering obstacles and increases the likelihood of REV getting out of "sticky" situations.

The suspension system is a four-bar lift designed to maximize the total sweep range. REV can lift each leg module up to one wheel diameter, or 0.25 m (10 in). The larger range allows for greater pitch and attitude adjustment ranges as well as increasing the obstacle height that REV can overcome. With the six-wheel configuration, a leg can be lifted while maintaining a stable chassis, whereas a four-legged chassis is susceptible to tipping. Conversely, a configuration greater than six wheels decreases the break-over angle due to the increased required length, which is not ideal for traversal over the rocky lunar terrain. Thus, the six-leg design was chosen for its balance of stability and mobility features.

REV is designed to use crab steering as the primary mode for traversing. With a 180° steering sweep range, wheels can be independently positioned to allow movement in any direction and rotation around any point. This allows REV to maneuver through tight spaces where conventional vehicles may struggle. Located at the end of the steer module, the drive motors are positioned off-axis to the drive axle to reduce the axial load on the gearbox. Each mechanism associated with its DOF is highlighted in Fig. 9.

Using this active suspension allows REV to maintain a level chassis on slopes and cross slopes. By using an IMU to measure the chassis orientation, REV can independently articulate each leg module to lean or prop its chassis. For instance, while climbing a slope of angle θ_{level}, REV can maintain a level chassis by extending and contracting its rear and front legs, respectively, as shown in Fig. 10. The maximum slope REV can climb while retaining a level chassis is a function of the length of the suspension arm and the total suspension sweep range. By increasing either of these parameters, the maximum slope increases. The same mechanics hold true for the cross-slope angle $\theta_{\text{level,cs}}$, as shown in Fig. 11. With its 0.25-m suspension range, REV can traverse through challenging slopes and cross slopes of 12° while maintaining a level chassis to transport RoboBall properly.

TABLE 2. REV and NASA JSC's Chariot comparison [18].

Parameter	REV	NASA Chariot
Payload Capacity	90 kg	1000 kg
Length	1.2 m	4.5 m
Active Suspension Range	0.25 m	0.635 m
Max Slope	12°	15°
Steering Range	180°	Continuous
Top Speed	10 km/hr	20 km/hr
Operating Voltage	12 V	336 V
Battery Composition	LiFePO4	Li-ion
Battery Configuration	3 Parallel	8 Series
Total Capacity	720 Wh @ 12 V	20.1 kWh @ 288 V

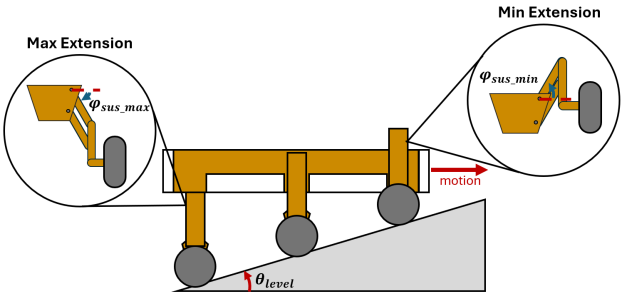

FIGURE 10. REV configuration that allows for chassis leveling during slope climb.

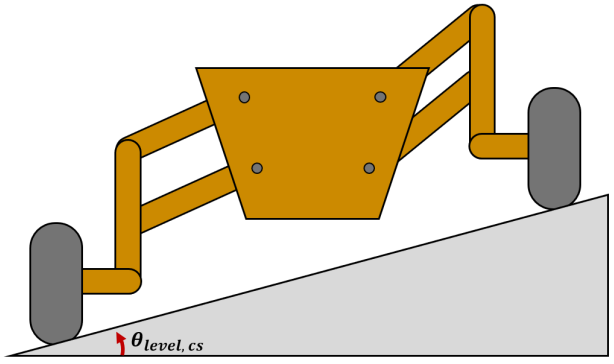

FIGURE 11. REV configuration that allows for chassis leveling during cross-slope climb.

Beyond this angle, REV cannot maintain a level chassis, but can climb a slope of up to 35°. Rover traction is a complex problem reliant on several parameters, including terramechanics and wheel geometry; as such, this calculation is based purely on the torque available to REV's wheels rolling without slipping on a flat incline.

C. ROBOBALL/REV INTEGRATION VIA AN ONBOARD CHARGING DOCK

The REV is outfitted with an inductive charger base designed to power RoboBall II while it is transported to the crater's

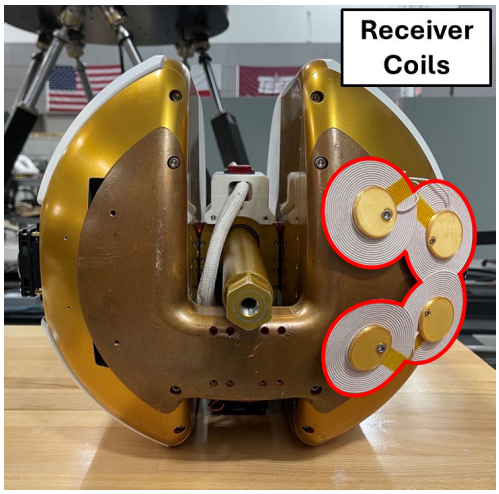

FIGURE 12. RoboBall II's pendulum base with its mounted receiver coils highlighted (outlined red).

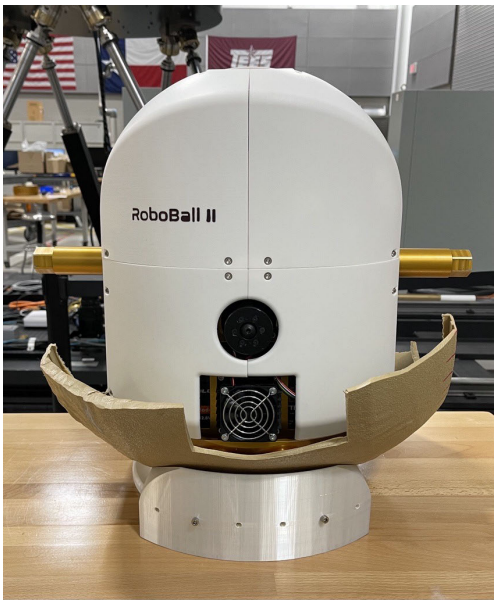

FIGURE 13. RoboBall II's inductive charger base and pendulum are mounted on its testing configuration.

edge. The charger is integrated into the rover's primary power system and also serves as a support cradle for RoboBall II during transit. The inductive charger is the key interface between the two robots, enabling seamless energy transfer that ensures RoboBall II remains operational without a direct electrical connection. RoboBall II is stored deflated to optimize charging efficiency, minimizing the distance between its receiver coils and the charger. Before its deployment, RoboBall II inflates by venting its onboard tanks and rolls off REV. A visualization of the charging system integrated onto REV, with RoboBall II positioned for charging, is shown in Fig. 1.

The charging base, as shown in Fig. 14, features a curved design with four overlapping coils to reduce the alignment

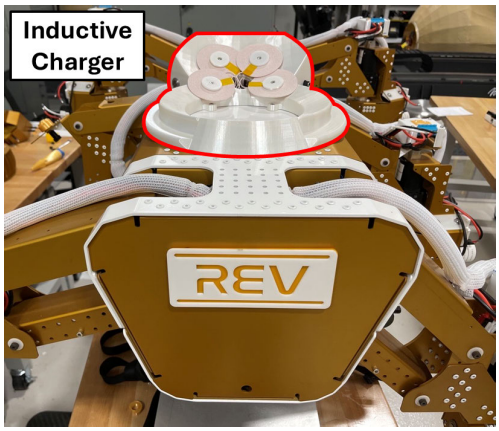

FIGURE 14. RoboBall II's inductive charging base (outlined red) shown integrated on the back of REV.

sensitivity during charging. It is securely bolted into the rover's main frame and is capable of maintaining a fully charged RoboBall II for over nine hours.

RoboBall II's receiver coils are located on the bottom of the internal pendulum, as shown in Fig. 12. These four coils are arranged to prevent interference with the shell's movement, with all coils concentrated on one side. The receivers are configured in two series pairs to double the voltage before being wired in parallel to increase the system's current. A battery management system steps down the 25 V from the receiver coils to a nominal 13.5 V before passing it through an in-line current sensor and into the RoboBall II battery relay. The placement of the coils at the bottom of the pendulum is crucial, as the high-strength elastomer shell allows the magnetic fields generated by the charger's transmitter to pass through with minimal interference. The asymmetrical receiver placement allows RoboBall to be deployed by tilting the unsupported side of REV, enabling a controlled release. The onboard current sensor provides real-time charge rate verification before the system proceeds to the next mission.

To validate the inductive charging system, the charging base, RoboBall II's pendulum, and a shell validation unit were mounted on a test bench, as shown in Fig. 14. The validation process included measuring the power transfer efficiency, charge rate, and alignment sensitivity under various conditions. First, the system's voltage and current were recorded at different receiver positions to assess alignment tolerance. The bowl-shaped charger base was shown to passively constrain RoboBall II's position, minimizing lateral displacement and limiting rotational movement to pitch and roll about the ball's center. To better understand how potential angular displacements affect charging performance, RoboBall II was incrementally tilted to a maximum $\pm 5^\circ$ in both axes to simulate misalignment from uneven terrain or rover motion. A power heatmap, as shown in Fig. 15, was generated showing the charging performance across these orientations. At optimal alignment, the charger maintained a stable charge rate of 2.2 A at 13.56 V. Notably, the charger's output exceeds

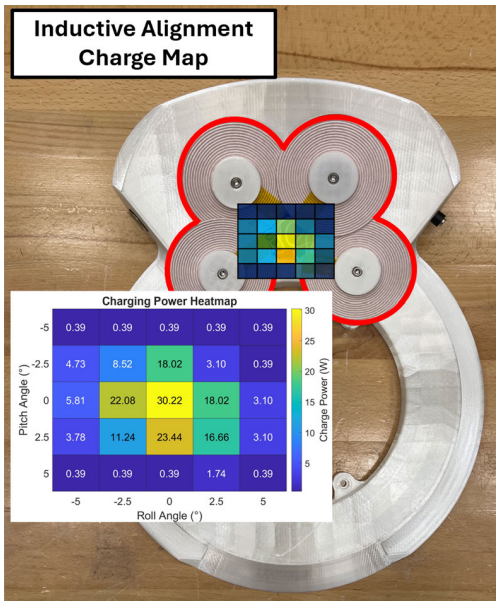

FIGURE 15. Heat map of power input to RoboBall II from REV-mounted inductive charger coils (outlined red) at varying levels of misalignment in RoboBall II's charger's centroid.

RoboBall II's idle power consumption of 20 W, ensuring the whole battery capacity is maintained. The heatmap revealed that RoboBall II sustains net positive charging within ±2° of both pitch and roll. Simultaneously, the power delivered to RoboBall II was compared to the power drawn from the test bench power supply to determine a system efficiency of 20.7%.

In addition, to determine the maximum slope abilities of the REV-RoboBall II combination, RoboBall II's mechanical stability while moving the cradle was analyzed. Static testing showed that roll angles above 8° and forward pitching above 12° resulted in charging alignment being affected. When the cradle and spherical robot were pitched back in the direction of the supported side of the cradle, effective charging was maintained up to 35° of incline. After these angles, the robot shifted significantly and would no longer be replenishing charge. The added mass of RoboBall also reduces REV's slope climbing capability to 30° in the ascent/descent directions. With the REV's 12° of slope leveling ability, this puts the maximum slope capabilities of the pair at 20° of roll in either direction, 24° of forward slope descent or 30° of slope ascent. These values are tabulated in Table 3.

These findings validate the inductive charger's ability to reliably power RoboBall II during transport and ensure operational readiness before deployment. As the REV and RoboBall II serve as analogs for the mission-capable Chariot and RoboBall III, these results provide insight into how the inductive charging system could be adapted for lunar applications. Scaling up the system would involve increasing power transfer capacity for the larger robots, such as the significantly larger capacity of Chariot (see Table 2) while maintaining efficiency in the lunar environment. Additional

TABLE 3. REV and RoboBall system slope traversal angle limitations.

Angle	Value (°)
REV Ascent/Descent (leveling)	12
REV Ascent/Descent	35
REV Roll (leveling)	12
REV Roll	12
REV + RoboBall Ascent	30
REV + RoboBall Descent	24
REV + RoboBall Roll	20

design considerations include optimizing coil configuration for higher power transfer due to the larger surface area on the bottom of RoboBall III and integrating autonomous coil alignment mechanisms to account for uneven terrain. Furthermore, the lunar gravity will provide increased performance to an REV-like rover's ability to transport a RoboBall, as the decreased weight reduces the load on the suspension motors.

As the REV is still under development, thorough field testing of the REV-RoboBall system could not be achieved. However, the preliminary results shown in this section, along with the physical interfacing of REV and RoboBall (as shown in Fig. 1) indicate that the integration of both robots is electrically and mechanically possible. Future testing, once REV is complete, would quantify charging efficacy and alignments as the rover transits across different terrains.

IV. SLOPE DESCENT

Although spheres naturally roll downhill, achieving controlled slope descent using RoboBall's internal 2-DOF pendulum is more complicated. This section focuses on the controller that enables RoboBall to descend 1-D slopes aligned with its forward axis. The goal of this section is to design and test a robust, simple slope descent controller that scales for both RoboBalls and avoids complicated control schemes such as gain scheduling or adaptive control.

Fig. 16 illustrates RoboBall's drive axis states and parameters relevant to descending a 1-D slope of angle α. Pravecek et al. [17] demonstrated that along the robot's forward axis, the pitch center and shell rotate together, while the pendulum moves independently but can be modeled relative to the shell's motion. In contrast, the pitch center and pendulum rotate about the robot's side axis. The angle of this rotation is known as the pitch angle γ. The shell spins independently with the drive shaft velocity ω. The pitch angle is measured using a VN-100 IMU rigidly mounted on the pitch center, while encoders on the drive motors measure the drive shaft velocity, also mounted on the pitch center. Consequently, ω is measured relative to the pitch center rather than with respect to the ground.

The free-body diagrams (FBDs) of the shell and the pendulum/pitch center can be found from Fig. 17, where τ_d is

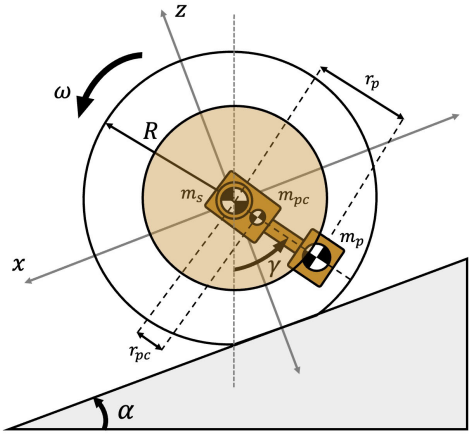

FIGURE 16. RoboBall's drive axis states and parameters relevant to slope descent.

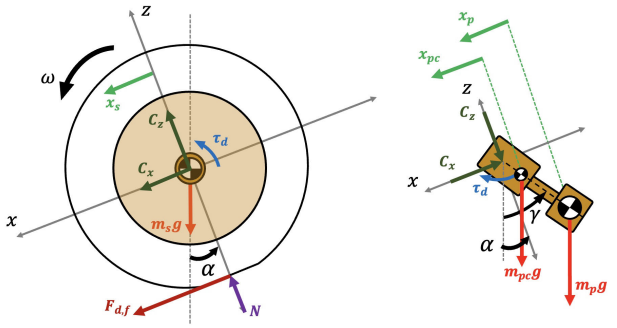

FIGURE 17. FBD of RoboBall's drive system separated into the shell and pendulum/pitch center links.

the actuator torque generated by the robot's drive motors. This torque acts on the shell, and its reaction torque acts on the pendulum/pitch center. The robot's drive axis nonlinear equations of motion (EOMs) while rolling down a slope are derived in the Appendix and presented in the standard robotics form in (A10). RoboBall's performance, particularly its slope traversal, depends significantly on the location of its center of gravity to provide the necessary reaction torque to the actuators. While this center of gravity provides less torque in a lunar gravity environment, the weight of the robot also decreases by the same factor, resulting in no performance loss.

The nonlinear dynamic model was analyzed at steady state to yield the static form of the system defined in (1). The torque τ_d is internal to the system and can be manipulated to define the form in (2), where the pitch angle γ is a function of the slope angle α

$$\begin{bmatrix} -\left(m_s + m_{\text{pc}} + m_p\right) Rg \sin(\alpha) \\ \left(m_{\text{pc}} r_{\text{pc}} + m_p r_p\right) g \sin(\gamma). \end{bmatrix} = \begin{pmatrix} \tau_d \\ -\tau_d \end{pmatrix} \tag{1}$$

$$\sin(\alpha) = \frac{m_{\text{pc}} r_{\text{pc}} + m_p r_p}{\left(m_s + m_{\text{pc}} + m_p\right) R} \sin(\gamma) = \frac{R_{\max}}{R} \sin(\gamma). \tag{2}$$

The slope angle and pitch angle relationship in (2) is used to generate a commanded pitch angle γ_{CMD} in (3) and a feedforward-gravity term δ_{slope} in (4) to compensate for the gravity terms that arise from a nonzero slope angle

$$\gamma_{\text{CMD}} = \arcsin\left(\frac{R}{R_{\max}} \sin(\alpha)\right) \tag{3}$$

$$\delta_{\text{slope}}(\alpha) = -\left(m_{\text{pc}} r_{\text{pc}} + m_p r_p\right) g \sin\left(\gamma_{\text{CMD}}(\alpha)\right). \tag{4}$$

The nonlinear dynamic model was linearized with the small-angle approximation applied to the state variables. The slope angle was also assumed to change slowly with respect to time, such that $\dot{\alpha}$ and $\ddot{\alpha}$ were assumed to be 0. Equation (5) shows the model linearized about operating points α_0 and γ_0. To express the linearized model in state-space form, the dynamics are written in terms of the augmented state vector $\boldsymbol{x}_d = \left[\omega\ \gamma\ \dot{\gamma}\right]^{\text{T}}$, resulting in a 3×3 mass matrix $\mathbf{M}_l$. The slope angle α is treated as an input disturbance and incorporated explicitly into the input matrix σ_l. The symbols used in this model are defined in the Appendix

$$\mathbf{M}_l(\alpha, \gamma)\dot{\vec{x}}_d + \mathbf{G}_l(\alpha, \gamma)\vec{x}_d = \sigma_d \vec{u}_d \tag{5}$$

where, $\mathbf{M}_l(\alpha, \gamma)$–$\vec{x}_d$, as shown at the bottom of the next page.

This linear model assumes small angular deviations, quasi-static slope variation and is linearized about fixed operating points α_0 and γ_0. This linear model and the nonlinear model presented form the basis for analyzing RoboBall's stability and control behavior during slope descent in the presence of slope perturbations.

Assuming the drive shaft spins slowly, adding the feedforward gravity compensation term δ_{slope}–τ_d approximately cancels the gravitational contribution in $\mathbf{G}_l(\alpha, \gamma)$ as well as the slope-induced input bias in σ_d, consistent with the model's quasi-static assumption. This feedforward term simplifies the linear system to the following model presented in the following equation:

$$\mathbf{M}_l(\alpha, \gamma)\dot{\vec{x}}_d + \begin{bmatrix} 0 & 0 & 0 \\ 0 & 0 & -1 \\ 0 & 0 & 0 \end{bmatrix} \vec{x}_d = \begin{bmatrix} 1 \\ 0 \\ -1 \end{bmatrix} \tau_d. \tag{6}$$

The simplified linear model is reorganized into a traditional state-space model in the following equation for control design purposes:

$$\dot{\vec{x}}_d = \mathbf{A}\vec{x}_d + \mathbf{B}\tau_d \tag{7}$$

where

$$\mathbf{A} = -\mathbf{M}_l^{-1} \begin{bmatrix} 0 & 0 & 0 \\ 0 & 0 & -1 \\ 0 & 0 & 0 \end{bmatrix} = \begin{bmatrix} 0 & 0 & \dfrac{I_{s,\text{eq}} - mrR\cos(\gamma_0 - \alpha_0)}{\Delta} \\ 0 & 0 & 0 \\ 0 & 0 & -\dfrac{I_{s,\text{eq}}}{\Delta} \end{bmatrix}$$

$$\mathbf{B} = \mathbf{M}_l^{-1}\begin{bmatrix}1\\-1\\0\end{bmatrix} = \begin{bmatrix}\frac{I_{p,\mathrm{eq}} - mrR\cos(\gamma_0-\alpha_0)}{\Delta}\\ -1\\ \frac{mrR\cos(\gamma_0-\alpha_0)}{\Delta}.\end{bmatrix}$$

$$\Delta = I_{s,\mathrm{eq}}I_{p,\mathrm{eq}} - (mrR\cos(\gamma_0-\alpha_0))^2.$$

This linear form was used to compute the linear quadratic regulator (LQR) optimal gains vector, $\mathbf{K_d}$, of the system with the weight matrices $\mathbf{Q}$ and $\mathbf{R}$ defined in (8). The weights along the diagonal of $\mathbf{Q}$ represent the weight for the state variables. Weight W_{τ_d} represents the weight applied to the control effort τ_d

$$\mathbf{Q} = \begin{bmatrix}W_\omega & 0 & 0\\ 0 & W_\gamma & 0\\ 0 & 0 & W_{\dot\gamma}\end{bmatrix}, \qquad \mathbf{R} = \begin{bmatrix}W_{\tau_d}\end{bmatrix}. \tag{8}$$

The model has been fully linearized about the operating points; however, since neither RoboBall II nor III can operate safely on slopes greater than 15° (as shown by Jangale et al. [16]), the slope angle α may be treated as small, and the nominal operating point α_0 can be assumed to be 0.

The γ_0 operating point is set to 0 to calculate offline the optimal gains vector for the drive axis for each robot, such that it can track velocity setpoints while operating on flat ground. Through simulation and testing, this gains vector alongside the slope compensation term proved to be effective in maintaining stability while descending slopes up to 20% grade (11.3°). However, the robot's ability to track velocity setpoints with zero error while descending slopes suffered. This could be improved by more advanced control techniques, such as gain-scheduling the components of $\mathbf{K_d}$ based on the slope angle and pitch angle, but would increase complexity.

The robot's driving control law is defined in (9). This controller is depicted in Fig. 18. Currently, RoboBall cannot actively measure the slope angle of the ground below it. As a result, the slope angle set point is either directly controlled by the robot's teleoperator with a joystick or manually set via the robot's command line. The RoboBall team is actively developing the live detection of slope angles and more complex slope maneuvering

$$\tau_d = \mathbf{K_d}\mathbf{e_d} + \delta_{\mathrm{slope}}(\alpha)$$

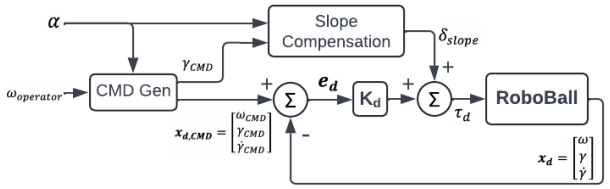

FIGURE 18. **Control diagram of RoboBall's slope descent algorithm using pitch angle and drive shaft velocity setpoint tracking.**

FIGURE 19. **RoboBall II (left) and RoboBall III (right) actively descending a 15% grade incline and a 20% grade incline using variations of the same controller.**

$$\mathbf{e_d} = \begin{bmatrix}\omega_{\mathrm{CMD}} - \omega\\ \gamma_{\mathrm{CMD}} - \gamma\\ \dot\gamma_{\mathrm{CMD}} - \dot\gamma\end{bmatrix}. \tag{9}$$

In Fig. 19, RoboBall II and RoboBall III are shown performing controlled descents on 15% (8.53°) and 20% grade, respectively [Appendix D1)]. Both robots use variations of the same feedback controller, each tuned for their respective dynamics.

Fig. 20 illustrates RoboBall II's drive system state response during its descent on a 15% grade incline. The experiment begins with one operator holding the robot in place while another sends the slope angle command. Once the command is received, the first operator releases the robot. In the "self-stabilizing" region, RoboBall II maintains its position under its own control. Descent begins when the operator increases the commanded drive velocity, prompting the robot to begin rolling. Since the gains are tuned for flat-ground behavior, a higher than-nominal velocity must be commanded to initiate motion.

$$\mathbf{M}_l(\alpha,\gamma) = \begin{bmatrix}I_{s,\mathrm{eq}} & 0 & I_{s,\mathrm{eq}} - mrR\cos(\gamma_0-\alpha_0)\\ 0 & 1 & 0\\ -mrR\cos(\gamma_0-\alpha_0) & 0 & I_{p,\mathrm{eq}} - mrR\cos(\gamma_0-\alpha_0)\end{bmatrix}$$

$$\mathbf{G}_l(\alpha,\gamma) = \begin{bmatrix}0 & 0 & 0\\ 0 & 0 & -1\\ 0 & mrg\cos(\gamma_0) & 0\end{bmatrix}$$

$$\sigma_d\vec{u}_d = \begin{bmatrix}1 & (m_s + m_{\mathrm{pc}} + m_p)Rg\\ 0 & 0\\ -1 & 0.\end{bmatrix}\begin{pmatrix}\tau_d\\ \alpha\end{pmatrix}$$

$$\vec{x}_d = \begin{pmatrix}\omega & \gamma & \dot\gamma\end{pmatrix}^{\mathrm{T}}$$

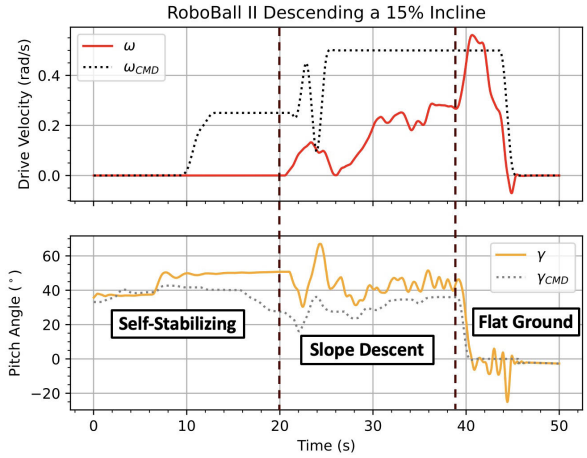

FIGURE 20. **Drive system state response of RoboBall II during a controlled 15% grade descent. Regions of the operator's interaction with the robot are labeled.**

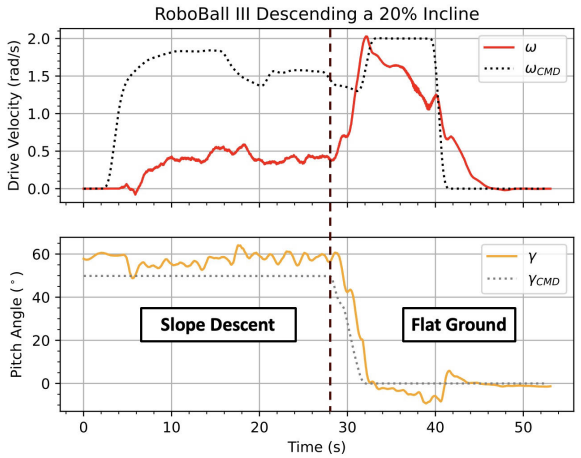

FIGURE 21. **Drive shaft velocity and pitch angle response of RoboBall III during a controlled 20% grade descent. Operator interaction regions are labeled.**

During the descent phase, the robot accelerates in a controlled manner until reaching an approximate steady-state velocity for approximately 10 s. Without active torque from the internal pendulum, this phase would exhibit unbounded drive shaft velocity and more chaotic pitch dynamics. Once the robot reaches the bottom of the slope, the slope descent command is canceled, and the commanded pitch angle returns to 0. RoboBall then regulates its drive velocity back to the setpoint before the operator cancels that command as well.

Fig. 21 shows the same experiment performed with RoboBall III on a 20% grade slope. Owing to its larger size and greater inertia, RoboBall III exhibits increased robustness to ground disturbances and more stable pitch dynamics during descent. During the slope descent phase, the robot maintains an angular drive velocity of approximately 0.5 rad/s, corresponding to a translational speed of roughly 0.46 m/s (1.5 ft/s). Compared with the shorter 15% grade incline, the extended length of the 20% grade allows for a clearer demonstration of the descent controller's performance in Fig. 21 than in Fig. 20.

V. BALLISTIC SAMPLE RETURN

While RoboBall excels at descending slopes, its ability to ascend slopes is limited [16]. Thus, any science or data collected must be independent of the robot's ability to exit the crater. In essence, RoboBall's ability to reach the bottom of a crater can be augmented with a sample return system, allowing for the collection of science and data samples from the depths of dangerous lunar craters without any significant risk to the primary rover and any operators. The ability to return a sample to outside the crater gives RoboBall a significant advantage over other proposed crater exploratory missions, as it increases the potential for more rigorous ex situ experimentation of samples, along with the potential to return samples to Earth with astronauts without the need for a separate, dedicated crater exploration mission.

To add this sample return capability to RoboBall III, the modularity of the robot's payload bay can be exploited. The sample acquisition and return rocket module (SARRM) was designed to be one of several modular systems that can be loaded into the annular payload bay of RoboBall III. To collect a sample, RoboBall III can lean over and extend the rocket. A sample acquisition system in the nose of the rocket can acquire the sample, at which point RoboBall III leans the other way and initiates the rocket launch, propelling the sample out of the crater. A diagram of the proposed collection process can be seen from Fig. 22. As the focus of this article is on the integration of this sample collection system with RoboBall, the details of any sample acquisition and processing are not discussed. However, systems such as a grabbing sampler or auger can be used as the nose of the rocket, especially since aerodynamics is not a factor in lunar operation [26]. For the purposes of demonstration, a nose cone with four scoops capable of collecting up to 3.35 cubic centimeters of a sample was used. Depictions of the SARRM system in CAD and the produced version loaded in RoboBall III's payload bay are shown in Figs. 23 and 24, respectively.

The SARRM system includes several onboard electronics. It contains a Raspberry Pi Zero W2 to enable wireless communication with RoboBall III's computer, allowing for RoboBall III to send commands to operate the module, e.g., launching the rocket. This Pi initiates a rocket launch via a command to a relay, which sends power to the rocket igniter. The module also has its own onboard power provided by an 11.1-V battery, which supplies the Pi, the rocket igniter, and any auxiliary electronics. The SARRM holds and can fire one 1.7 m, 250 g (5.6 ft, 0.55 lb) rocket; the rocket used is a slightly modified Estes Mean Machine model rocket used as a placeholder. Estes E16 class rocket motors, though underpowered for this application, were used to constrain the distance of the rocket within testing grounds and for operational safety. With a total impulse of 33 N·s, the maximum

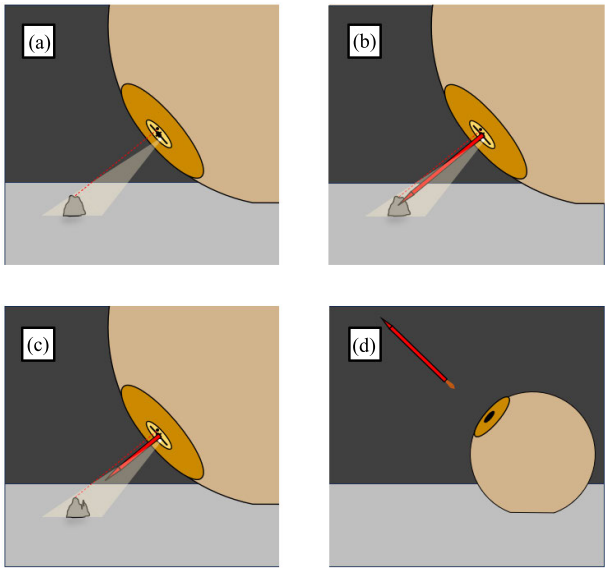

FIGURE 22. (a) RoboBall locates a sample using the SARRM camera. (b) RoboBall collects a sample. (c) SARRM rocket is prepped for launch. (d) RoboBall steers to the desired launch angle and uses the onboard camera to aim in the direction of REV. The rocket is launched, and the sample is ejected from the crater.

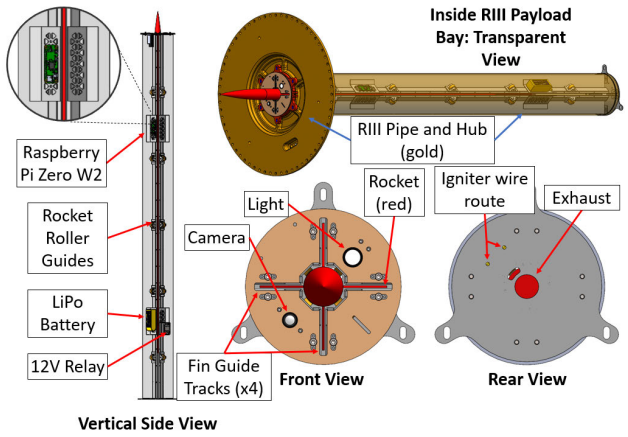

FIGURE 23. CAD model of the SARRM with electronics, multiple views.

effective range of this rocket in lunar gravity is about 8.2 km (5.1 mi) and a max total height of approximately 4.0 km (2.5 mi), allowing for the robot to propel a sample outside a crater like the Shackleton crater from within most of the crater and from its deepest points [27]. A total impulse of 38 N·s is required to exceed the crater radius of 11 km (6.8 mi), which is easily achievable through larger commercially available solid rocket motors, such as F15 rocket motors with their total impulse of 49.6 N·s. A comparison of valid launch zones between these two motors can be seen from Fig. 25.

VI. SAMPLE RECOVERY DESIGN

It is desirable for the SARRM to land near REV. This eases the recovery of the sample and increases the number of

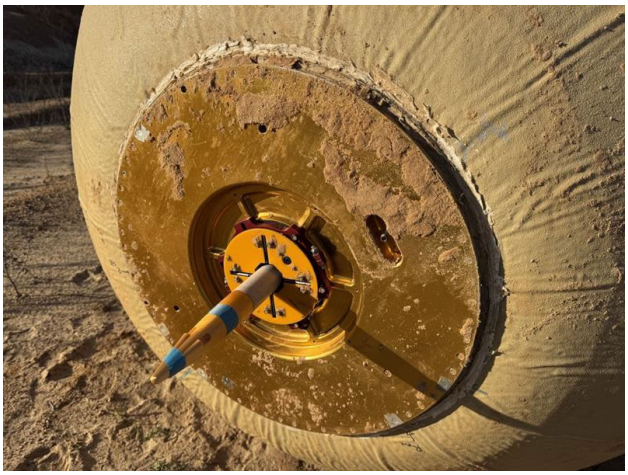

FIGURE 24. SARRM system was loaded in RoboBall III's payload bay in the field.

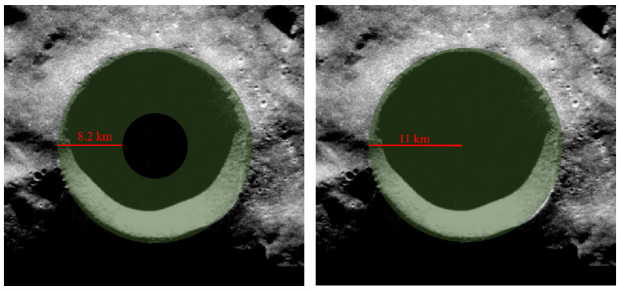

FIGURE 25. Valid launch zones of the SARRM system with E16 motors (left) and F15 or higher motors (right) in shackleton crater.

missions a singular REV will accomplish. Possible solutions will be considered for planning the initial trajectory of the launch and tracking the SARRM once it has landed. These solutions will likely need to be modified as they involve systems that are planned for but not yet implemented.

NASA has proposed LunaNet as the infrastructure to enable lunar operations by acting as a service network for communications and navigation [28]. LunaNet comprises nodes acting as network access points similar to terrestrial cell towers. Each node will communicate through a common language architecture and partake in inter-nodal communication. This network will comprise multiple orbiting and stationary nodes on the lunar surface, granting near-constant communication with any other user. REV could act as an access point for RoboBall as RoboBall descends into the crater. RoboBall can then utilize positional updates from this network to find the proper launch heading.

Utilizing the onboard camera can act as a secondary check for the launch heading. RoboBall could match astral maps of the stars to find their relative position and launch heading from the bottom of the crater. The shadowed bottom of the crater will prevent the contrast that generally inhibition this on most of the lunar surface. NASA has mapped the

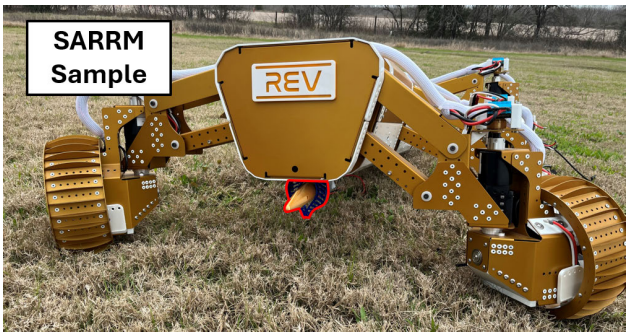

FIGURE 26. REV holding the SARRM rocket sample collector (outlined red) via two compliant finger modules.

Shackleton crater using the Lunar Reconnaissance Orbiter and modeled how sunlight moves around the rim of the crater [29]. RoboBall could determine the launch heading based on the known sunlight patterns along the rim.

To further increase the accuracy of the rocket, REV could update the trajectory after the launch. Utilizing LunaNet, and with REV acting as a ground station, the rocket could utilize real-time kinematic (RTK) positioning akin to large-scale drone shows. Research has shown that centimeter accuracy can be achieved with a single ground station [30]. The absence of atmospheric interference means an accurate final trajectory could be calculated from two timestamped positional updates. To account for any inconsistency from the landing, REV could utilize received signal strength comparison to pinpoint the final location of the sample collector [31].

To collect the sample, a simple parallel jaw end-effector equipped with two compliant fingers attached to the underside of REV could be used. To grab the sample, REV can crouch over the sample, close the end-effector, and stand up so that the sample no longer touches the ground. REV could then return to base camp with the rocket under the main body, as highlighted in Fig. 26.

VII. MISSION DESIGN

By integrating all of the previously discussed components, a potential mission can be formulated. By utilizing the strengths of each robot, a mission flowchart can be seen from Fig. 27.

A. MISSION PLAN

The detailed mission steps from Fig. 27 are described below.

1) *Mission Start:* The rover (NASA Chariot, analog: REV) is deployed to the lunar surface. It carries onboard a RoboBall (RoboBall II/RoboBall III) equipped with an SARRM system.
2) *Rover Navigates General Terrain*: The rover travels from the landing site toward the desired crater. Along the way, the rover can conduct additional science experiments on the lunar surface as well as collect navigational data. RoboBall remains stored and uses the inductive charger to stay at full capacity.
3) *Rover Approaches Desired Crater:* The rover, having completed auxiliary missions, approaches the desired crater, e.g., Shackleton crater. RoboBall prepares for deployment and performs checks on systems, including pressure, battery level, and SARRM connectivity.
4) *Rover Deploys RoboBall at Crater Edge:* As the rover approaches the crater lip, RoboBall drives off of rover into the crater. A mock-up of this interaction using REV and RoboBall II is shown in Fig. 1.
5) *RoboBall Descends Crater:* RoboBall begins its descent down the walls of the crater. RoboBall attempts to use a controlled slope descent using the controller described in Section IV to the best of its ability, and bounces in an uncontrolled manner when unable, eventually reaching the bottom of the crater.
6) *RoboBall Traverses Crater Interior:* After righting itself postdescent, RoboBall travels along the bottom of the crater to a desired sampling location, navigating via teleoperation from outside the crater, or potentially via preprogrammed heading commands.
7) *RoboBall Acquires Sample With SARRM:* As RoboBall approaches the desired sampling area, it collects a sample using the SARRM with the process described in Section V. A sample is chosen with the onboard SARRM camera, which can be replaced with alternative sensing equipment based on desired sample characteristics.
8) *RoboBall Uses SARRM to Return Sample:* Using the onboard camera of the SARRM along with any of the potential localization and navigation techniques discussed in Section VI, RoboBall orients and fires the sample out of the crater in the direction of the rover to facilitate recovery.
9) *Rover Collects the Sample:* The rover locates and acquires the sample using several potential methods. If autonomous and uncrewed, the rover can utilize a variety of manipulation techniques, such as those described in Section VI. If crewed, an astronaut can recover the sample without the associated risk of approaching a crater.
10) *Mission End:* With the sample collected, the rover is free to depart and take the sample for analysis. RoboBall is discarded. By exploiting the strengths of each robot, a sample from the depths of a crater was safely extracted with neither risk to any potential human operators nor risk of failing any greater mission by compromising the primary rover.

B. MISSION ANALOG

In order to validate the performance of the RoboBall paradigm in crater descent, an analog of the mission was conducted in a quarry. The quarry used was 200 m (656 ft) in diameter with an average grade of approximately 25%. While not as soft as lunar regolith, this quarry had relatively soft and clay soil, which helped validate RoboBall's performance outside of the concrete conditions shown in Section IV. The

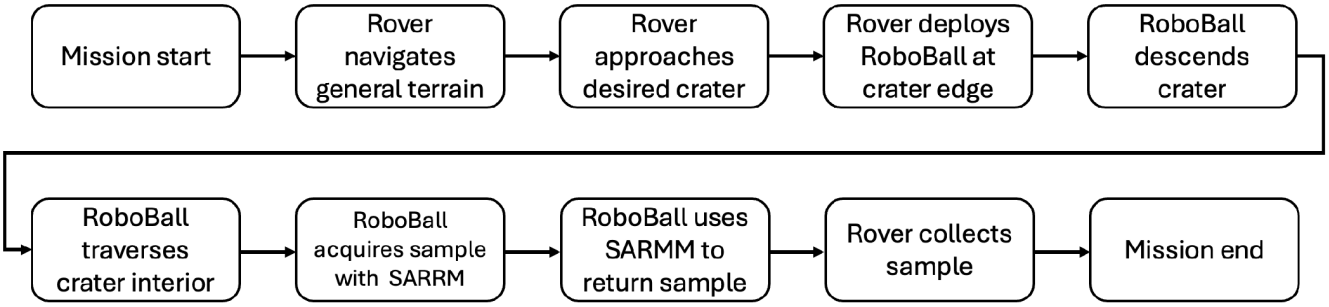

FIGURE 27. **Flowchart of the proposed mission.**

FIGURE 28. **An aerial view of RoboBall III being deployed from Oshkosh HEMTT near crater.**

REV rover was not yet available for field testing as it is still under development. As such, the field testing of the proposed REV-RoboBall II and its transportation synergy was limited in scope, as discussed in Section III. Furthermore, as access to NASA's Chariot rover (which would be the actual mission vehicle) was not available for testing, the RAD Lab's Oshkosh Heavy Expanded Mobility Tactical Truck (HEMTT) 10 × 10 PLS was used as an alternative roving vehicle, seen loaded with RoboBall III in Fig. 28. Doing so allowed for the crater descent validation of the RoboBall III platform.

RoboBall III was then driven via teleoperation into the crater with an SARRM system in the payload bay. Though the robot is robust enough to roll and bounce uncontrolled due to its shape and soft shell, the slope descent controller was utilized to attempt a controlled descent where possible. While the controlled descent with minimal acceleration is ideal, uncontrolled bouncing coupled with the periodic controlled descent will still decrease the risk of fatal impact to the robot by reducing overall speed and acceleration during descent as opposed to purely uncontrolled descent. The ability to perform uncontrolled descent is still a major advantage over traditional wheeled rovers, which are less poised to survive such a descent. The robot successfully descended to the crater via the described motion five times. Each test run was approximately 110 m, (360 ft) with an average slope of 25%. For each of these tests, mission time, power consumed, and resulting cost of transport with respect to mass and distance

TABLE 4. **RoboBall III mission analog test metrics.**

Test	Mission Time (sec)	Power Consumed (Wh)	Percentage Power Used (%)	Cost of Transport ($\frac{Wh}{m \cdot kg}$)
1	721	25.3	3.1	1.49e-3
2	705	28.9	3.5	1.70e-3
3	840	23.4	2.9	1.38e-3
4	460	16.4	2.0	1.0e-3
5	312	7.0	0.9	4.0e-4
Mean	607.6	20.2	2.5	1.2e-3
Std. Dev.	215.4	8.7	1.0	5.0e-4

FIGURE 29. **RoboBall III descends the analog crater.**

were calculated. As RoboBall III uses AGM batteries, which can tolerate a depth of discharge of 80%, the actual capacity of the robot used to compare power usage is 80% of the theoretical capacity, or 806.4 W·h at 48 V. Performance metrics of each test run can be found from Table 4. An image of the robot descending the crater during the first run is shown in Fig. 29.

As shown, the robot is extremely efficient in performing its descent, using at most 3.5% battery. The fourth and fifth runs opted for a substantially less conservative tele-operation approach to descent by utilizing increased velocity and momentum, resulting in a substantially lower descent time and a decreased power cost. Despite the more dynamic and impact-laden descent, the robot remained fully operational

TABLE 5. RoboBall III sample return metrics.

Launch	Distance Traveled (m)
1	241
2	107
3	139
4	154
5	124
Mean	153
Std. Dev.	52.2

after these tests. Modifications to double the battery capacity of RoboBall III by changing battery chemistry are currently being developed, which will reduce the overall percentage of power consumed and increase the robot's effective range. It is important to note that RoboBall is currently unable to perceive the exact slope it is actively on. As such, the average slope of the overall descent path was used to minimize acceleration. Knowledge of the current slope would facilitate a more controlled descent.

At the bottom of the quarry, SARRM was used to collect samples of soil weighing approximately 1.5 g. RoboBall III was then maneuvered to face closer to the HEMTT and steered to aim the SARRM at a launch angle of 35°. The SARRM rocket was then fired, ejecting the sample outside the crater limits. To attempt to minimize wind interference, launches were performed near dawn. A five total launches were conducted, as seen in Table 5.

Deliberately underpowered D12 engines were used for safety and to ensure the rocket stayed within range of the operators for retrieval. With this engine configuration, the sample was found 26 m (85 ft) away from the HEMTT and 241 m (791 ft) from the launch site after a near perfect, zero-wind first launch, validating RoboBall's ability to descend a crater and return samples. Subsequent launches were subject to a headwind and may have affected the consistency of the rocket's range. Images of RoboBall completing sampling and return from external and SARRM views are shown in Fig. 30.

An average mission path between multiple runs is shown in Fig. 31, where the gold dotted line represents the RoboBall path and the red dotted line represents the SARRM rocket path.

1) NOTE

For safety reasons and to adhere to local and testing facility regulations, a live rocket was not loaded in the SARRM until the robot had stopped at the bottom of the quarry. Furthermore, while SARRM is capable of firing the rocket using onboard electronics, a manual firing sequence was used to ensure the safety of operators, bystanders, and the environment.

VIII. LESSONS LEARNED

Throughout the design and experiment process, several observations were made that will affect future development of this mission concept.

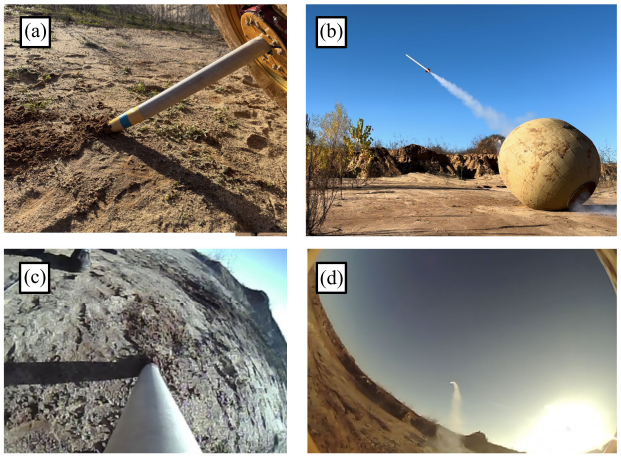

FIGURE 30. (a) RoboBall III with the SARRM rocket "collecting" a sample. (b) RoboBall III firing the SARRM rocket to the HEMTT. (c) SARRM view of (a). (d) SARRM view of (b)

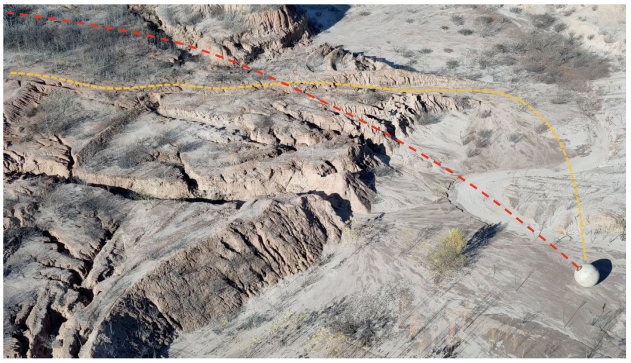

FIGURE 31. Average path followed by RoboBall III (gold dotted line) and by the SARRM rocket (red dotted line) in analog mission between multiple runs.

When developing the rover-spherical robot interaction, the advantages and disadvantages of inductive charging became apparent. While effective in charging the RoboBall through its shell, the charger's efficiency can be significantly impacted by misalignment, affecting the rover's ability to effectively transport the RoboBall to its mission destination. Furthermore, limitations in the RoboBall II cradle's ability to contain the ball constrain REV's slope traversal capabilities. However, increasing the rim of the cradle would make it more difficult for RoboBall to disembark, which warrants increased consideration in cradle design alongside more active alignment features for RoboBall III.

Furthermore, while RoboBall can compensate for descent on known slopes, it is currently unable to perceive and adapt to its active slope, as well as cross slopes. As the slope is often not consistent locally in off-road terrain, a rough estimate of slope may prove useful.

Finally, RoboBall III proved more robust than anticipated at chaotic descent, and as power consumption seems to decrease by adopting faster descent, there is value in testing

the limits of RoboBall III's ability to survive drops and slopes. This, combined with increases to torque and robustness of the robot's drivetrain, will allow for better mission planning.

Due to the lengthy experimental timelines and the strong dependence on favorable weather conditions, further testing could not be conducted within the present study. Furthermore, as the REV is in early development, the REV-RoboBall interaction could not be validated in the field. While these results are preliminary, they demonstrate promising trends that warrant more rigorous testing in future studies. A potential expanded testing campaign would involve quantifying charging efficacy and overall transport efficiency with REV and RoboBall II system, as well as adaptation of their respective interactive features to RoboBall III and its rover stand-in. More rigorous testing of RoboBall III in varying crater terrains would help to develop the full range of RoboBall's crater descent capabilities. Finally, the implementation of onboard sensors and vision would allow for more effective use of the slope controller discussed in Section IV, reducing uncontrolled descent.

IX. CONCLUSION

In this article, a collaborative multirobot team for lunar crater exploration was proposed. Individual actors within this team were analyzed, and novel components, such as a slope descent controller, were proposed. Robot enhancements to augment mission capabilities in the form of a sample return module were discussed. Finally, a mission plan was developed, and an analog of the mission was conducted in a terrestrial mock crater. Preliminary results indicate that integration between the REV and RoboBall can prove effective. Isolated testing of the RoboBall platform also validated the robustness of the robot in a preliminary off-terrain environment.

Future work will involve exploring complex mobility techniques for the REV rover. Increased autonomy in the RoboBall paradigm will also be considered, including adding real-time slope detection via the addition of payload modules with more advanced sensing. REV/RoboBall II interaction systems, such as the inductive charger, will be adapted to RoboBall III, while also being tested on REV in the field. RoboBall III's mobility capabilities will be expanded to allow for greater robustness, while validating the system on a greater variety of terrains. Finally, robust rocket recovery mechanisms for REV, such as a manipulator, will be explored.

APPENDIX

A. ROBOBALL SLOPE DESCENT DYNAMIC MODEL DERIVATION

Fig. 17 illustrates the planar FBDs of the shell and the pitch center/pendulum. The shell, pitch center, and pendulum have mass moments of inertia $I_{s,y}$, $I_{\mathrm{pc},y}$, and $I_{p,y}$, respectively, about the robot's y-axis. The relevant kinematic relationships for deriving the RoboBall's slope descent model are given in (A1)–A3, where r_{pc} and r_p are the moment arms of the pitch center's and pendulum's offset masses respectively,

$$\dot{x}_s = R\left(\omega + \dot{\gamma}\right) \tag{A1}$$

$$x_{\mathrm{pc}} = x_s - r_{\mathrm{pc}} \sin\left(\gamma - \alpha\right) \tag{A2}$$

$$x_p = x_s - r_p \sin\left(\gamma - \alpha\right). \tag{A3}$$

The shell's rotational equation of motion is defined in (A4), where $F_{d,f}$ is the rolling frictional force with a rolling without slipping condition in the drive direction and R is the shell's radius

$$I_{s,y}\left(\dot{\omega} + \dot{\gamma}\right) = \tau_d - \mathrm{RF}_{d,f}. \tag{A4}$$

The translational EOMs for the shell (mass m_s) and the pendulum/pitch center (masses m_p and m_{pc}) are given in (A5) and (A6), where C_x denotes the internal force acting along the x-axis at the pitch joint

$$m_s\ddot{x}_s = C_x + F_{d,f} + m_{\mathrm{sg}} \sin\left(\alpha\right) \tag{A5}$$

$$m_{\mathrm{pc}}\ddot{x}_{\mathrm{pc}} + m_p\ddot{x}_p = -C_x + \left(m_{\mathrm{pc}} + m_p\right) g \sin\left(\alpha\right). \tag{A6}$$

Equations (A5) and (A6) can be combined to solve for $F_{d,f}$ defined in (A7)

$$\begin{aligned} F_{d,f} = {} & m_s\ddot{x}_s + m_{\mathrm{pc}}\ddot{x}_{\mathrm{pc}} + m_p\ddot{x}_p \\ & - \left(m_s + m_{\mathrm{pc}} + m_p\right) g \sin\left(\alpha\right). \end{aligned} \tag{A7}$$

Equation (A7) and the appropriate time derivatives of the kinematic relationships can be substituted into (A4) to yield the system's first state equation defined in (A8). The time derivatives of the kinematic relationships are formulated to account for the slope's angle changes over time

$$\begin{aligned} & I_{s,\mathrm{eq}}\dot{\omega} + \left(I_{s,\mathrm{eq}} - mrR\cos\left(\gamma - \alpha\right)\right)\ddot{\gamma} \\ & + mrR\cos\left(\gamma - \alpha\right)\ddot{\alpha} + mrR\sin\left(\gamma - \alpha\right)\left(\dot{\gamma} - \dot{\alpha}\right)^2 \\ & - \left(m_s + m_{\mathrm{pc}} + m_p\right) Rg \sin\left(\alpha\right) = \tau_d \end{aligned} \tag{A8}$$

where

$$\begin{aligned} I_{s,\mathrm{eq}} &= I_{s,y} + \left(m_s + m_{\mathrm{pc}} + m_p\right) R^2 \\ mr &= m_p r_p + m_{\mathrm{pc}} r_{\mathrm{pc}}. \end{aligned}$$

Carrying out the moment balance of the pendulum/pitch center FBD yields the second state equation defined in (A9)

$$\begin{aligned} & \left(I_{p,\mathrm{eq}} - mrR\cos\left(\gamma - \alpha\right)\right)\ddot{\gamma} - mrR\cos\left(\gamma - \alpha\right)\dot{\omega} \\ & + mrg\sin\left(\gamma\right) = -\tau_d \end{aligned} \tag{A9}$$

where

$$I_{p,\mathrm{eq}} = I_{p,y} + m_p r_p^2 + I_{\mathrm{pc},y} + m_{\mathrm{pc}} r_{\mathrm{pc}}^2.$$

Equations (A8) and (A9) are the nonlinear EOMs that reflect the motion of RoboBall's states when descending slopes of time-variant slope angle. These EOMs are represented in matrix form in the standard robotic form defined in (A10), where the drive velocity states are defined as $\vec{\boldsymbol{\omega}}_d = \left[\omega, \dot{\gamma}\right]^{\mathrm{T}}$

$$\mathbf{M}\left(\alpha, \gamma\right)\dot{\vec{\boldsymbol{\omega}}}_d + \vec{\mathbf{c}}\left(\alpha, \dot{\alpha}, \gamma, \dot{\gamma}\right) + \vec{\mathbf{g}}\left(\alpha, \gamma\right) = \begin{pmatrix} \tau_d \\ -\tau_d \end{pmatrix} \tag{A10}$$

where

$$\mathbf{M}(\alpha,\gamma)=\begin{bmatrix} I_{s,\text{eq}} & I_{s,\text{eq}}-mrR\cos(\gamma-\alpha) \\ -mrR\cos(\gamma-\alpha) & I_{p,\text{eq}}-mrR\cos(\gamma-\alpha)\end{bmatrix}$$

$$\vec{\boldsymbol{c}}(\alpha,\dot{\alpha},\gamma,\dot{\gamma})=\begin{bmatrix} mrR\sin(\gamma-\alpha)(\dot{\gamma}-\dot{\alpha})^2 \\ 0\end{bmatrix}$$

$$\vec{\mathbf{g}}(\alpha,\gamma)=\begin{bmatrix} -\left(m_s+m_{\text{pc}}+m_p\right)Rg\sin(\alpha) \\ mrg\sin(\gamma)\end{bmatrix}.$$

B. SARRM ROCKET RANGE ESTIMATION

To estimate the efficacy of the SARRM in lunar gravity, first principles calculations were done to estimate the range of a rocket, and to ascertain any required modifications required to the rocket motor. Due to the usage of rollers that constrain the rocket from touching the tube and rolling with the rocket as it is fired, friction can be neglected. Assuming usage of an Estes E16 class rocket motor with a total impulse of 33.68 N·s, the velocity of the rocket post burn, v_{pb}, is seen in (B1)

$$v_{\text{pb}}=\frac{I}{M_{\text{total}}}. \tag{B1}$$

Using this final velocity, the kinematic relation for horizontal range x_{total} in a parabolic flight was used, as shown in (B2). A launch angle θ of 45° was assumed, as this would maximize the flight range. g_l is the lunar gravity of 1.63 m/s^2

$$x_{\text{total}}=\frac{v_{\text{pb}}^2\sin(2\theta)}{g_l}. \tag{B2}$$

With the parameters relevant to the E16 rocket motor and launch angle, a maximum range of approximately 8.2 km was estimated. To obtain a distance of 11 km, the shown equations were solved backward to determine the required 39-N·s impulse.

C. ESTIMATED SLOPE CONVERSION

In order to scale the efficacy of the robot on slope descent on the lunar surface, an equivalent terrestrial angle was estimated with some simplifying assumptions.

Assuming a spherical robot with a given mass, rotational inertia, and geometric parameters is rolling without slipping down a smooth incline of angle β on the lunar surface of a fixed length, the equivalent angle that induces the same acceleration for the same length can be found as follows, where g is the Earth's gravitational constant, α is the equivalent angle of the slope on Earth, and β is the lunar incline angle

$$g\sin(\alpha)=\frac{g}{6}\sin(\beta). \tag{C1}$$

From this, an example lunar incline β of 30° can be chosen, as this corresponds roughly to regions of the Shackleton crater rim as measured by orbital measurements [27]. The equivalent angle α on Earth is approximately 4.8°.

When considering the descent scheme of uncontrolled descent with periodic controlled descent to limit velocity, this implies that, on the Moon, RoboBall can perform an uncontrolled descent for approximately six times as long before a controlled descent maneuver must be performed to reduce the robot's velocity.

D. MULTIMEDIA README

1) *RoboBall III Slope Descent:* www.youtube.com/watch?v=cP7r6An7S6o. In this video, a controlled descent of RoboBall III using the controller described in Section IV on 20% grade is shown.
2) *Crater Test Run 1:* https://youtu.be/FW3dTuW4cDs. In this video, the first of three test runs of RoboBall III's slope descent in a mock crater can be seen. The second test run is virtually identical and offers no meaningful contribution.
3) *Crater Test Run 3:* https://youtu.be/-Hlh6a7VHh8. In this video, the third of three test runs of RoboBall III's slope descent in a mock crater can be seen.

ACKNOWLEDGMENT

The authors would like to thank Jimmy Massey, Jared Byars, Retvin Pant, and Sarah Toomes for their support during the field testing of the robots discussed.

REFERENCES

[1] T. Aoki, Y. Murayama, and S. Hirose, "Mechanical design of three-wheeled lunar rover; 'Tri-star IV,'" in *Proc. IEEE Int. Conf. Robot. Autom.* Shanghai, China, May 2011, pp. 2198–2203.
[2] N. Kingry, Y.-C. Liu, M. Martinez, B. Simon, Y. Bang, and R. Dai, "Mission planning for a multi-robot team with a solar-powered charging station," in *Proc. IEEE/RSJ Int. Conf. Intell. Robots Syst. (IROS)*, Sep. 2017, pp. 5233–5238.
[3] P. S. Schenker, T. L. Huntsberger, P. Pirjanian, E. T. Baumgartner, and E. Tunstel, "Planetary rover developments supporting Mars exploration, sample return and future human–robotic colonization," *Auto. Robots*, vol. 14, nos. 2–3, pp. 103–126, Mar. 2003.
[4] R. Prakash et al., "Mars science laboratory entry, descent, and landing system overview," in *Proc. IEEE Aerospace Conf.*, Big Sky, MT, USA, Mar. 2008, pp. 1–18.
[5] M. Duggan, X. Simon, and T. Moseman, "Lander and cislunar gateway architecture concepts for lunar exploration," in *Proc. IEEE Aerosp. Conf.*, Big Sky, MT, USA, Mar. 2019, pp. 1–9.
[6] K.-J. Kim, B.-S. Sim, S.-H. Kim, and K.-H. Yu, "Wheel design methodology for a lunar exploration rover in order to improve trafficability considering operation environment," in *Proc. IEEE Int. Conf. Robot. Autom. (ICRA)*, May 2018, pp. 904–909.
[7] H. Nakashima et al., "Discrete element method analysis of single wheel performance for a small lunar rover on sloped terrain," *J. Terramechanics*, vol. 47, no. 5, pp. 307–321, Oct. 2010.
[8] X. Yu, Z. Deng, H. Fang, and J. Tao, "Research on locomotion control of lunar rover with six cylinder-conical wheels," in *Proc. IEEE Int. Conf. Robot. Biomimetics*, Jun. 2006, pp. 919–923.
[9] J. Zhang, Z. Liu, and Z. Qin, "Passive suspension design and dynamics analysis of manned lunar rover," in *Proc. 10th Int. Conf. Mechatronics Robot. Eng. (ICMRE)*. Milan, Italy, Feb. 2024, pp. 155–160.
[10] R. A. Lindemann and C. J. Voorhees, "Mars exploration rover mobility assembly design, test and performance," in *Proc. IEEE Int. Conf. Syst., Man Cybern.*, Jul. 2005, pp. 450–455.
[11] S. Shrivastava et al., "Material remodeling and unconventional gaits facilitate locomotion of a robophysical rover over granular terrain," *Science Robotics*, vol. 5, no. 42, 2020, Art. no. eaba3499.
[12] F. Cordes et al., "An active suspension system for a planetary rover," in *Proc. Int. Symp. Artif. Intell.*, Jun. 2014, pp. 17–19.
[13] D. Loret de Mola Lemus, D. Kohanbash, S. Moreland, and D. Wettergreen, "Slope descent using plowing to minimize slip for planetary rovers," *J. Field Robot.*, vol. 31, no. 5, pp. 803–819, Sep. 2014.

[14] B. Bluethmann et al., "An active suspension system for lunar crew mobility," in *Proc. IEEE Aerosp. Conf.*, Big Sky, MT, USA, Mar. 2010, pp. 1–9, doi: 10.1109/AERO.2010.5446895. [Online]. Available: http://ieeexplore.ieee.org/document/5446895/
[15] M. Oevermann, D. Pravecek, G. Jibrail, R. Jangale, and R. O. Ambrose, "RoboBall: An all-terrain spherical robot with a pressurized shell," in *Proc. IEEE Int. Conf. Robot. Autom. (ICRA)*, May 2024, pp. 13502–13508.
[16] R. V. Jangale et al., "Scaling of RoboBall: A parametric robot family for Crater exploration," in *Proc. IEEE Aerosp. Conf.*, Mar. 2025, pp. 1–8.
[17] D. J. Pravecek, M. J. Oevermann, G. C. Thomas, and R. O. Ambrose, "Empirically compensated setpoint tracking for spherical robots with pressurized soft-shells," *IEEE Robot. Autom. Lett.*, vol. 10, no. 3, pp. 2136–2143, Mar. 2025, doi: 10.1109/LRA.2025.3527308.
[18] D. A. Harrison, R. Ambrose, B. Bluethmann, and L. Junkin, "Next generation rover for lunar exploration," in *Proc. IEEE Aerosp. Conf.*, Mar. 2008, pp. 1–14, doi: 10.1109/AERO.2008.4526234.
[19] M. Oevermann, R. O. Ambrose, and M. P. Dravid, "A soft spherical robot for lunar Crater exploration," in *Proc. AIAA SCITECH Forum*, Jan. 2024, p. 1961.
[20] M. J. Oevermann, M. P. Dravid, D. J. Pravecek, W. Olejnik, and R. O. Ambrose, "A pressure model and control system for a pressurized pendulum driven spherical robot," in *Proc. 22nd Int. Conf. Ubiquitous Robots (UR)*, Jun. 2025, pp. 426–431.
[21] M. Roozegar and M. J. Mahjoob, "Modelling and control of a non-holonomic pendulum-driven spherical robot moving on an inclined plane: Simulation and experimental results," *IET Control Theory Appl.*, vol. 11, no. 4, pp. 541–549, Feb. 2017.
[22] H. Kolbari, A. Ahmadi, M. Bahrami, and F. Janati, "Impedance estimation and motion control of a pendulum-driven spherical robot," in *Proc. 6th RSI Int. Conf. Robot. Mechatronics (IcRoM)*, Oct. 2018, pp. 6–11.
[23] M. Nagai, "Control system for a spherical robot," Master's thesis, Dept. Space Sci., Lulea Univ. Technol., 2008, p. 116.
[24] D. Magree et al., "Georgia tech team entry for the 2013 AUVSI international aerial robotics competition," Amer. Inst. Aeronaut. Astronaut., Georgia Inst. Technol., Tech. Rep., 2013.
[25] (Dec. 2024). *NASA Prepares For Lunar Terrain Vehicle Testing*. [Online]. Available: https://www.nasa.gov/humans-in-space/nasa-prepares-for-lunar-terrainvehicle-testing/
[26] T. Zhang et al., "The progress of extraterrestrial regolith-sampling robots," *Nature Astron.*, vol. 3, no. 6, pp. 487–497, Jun. 2019, doi: 10.1038/s41550-019-0804-1.
[27] R. V. Wagner et al., "Topography of 20-km diameter Craters on the moon," in *Proc. Lunar Planetary Sci. Conf.*, vol. 44, 2013, p. 2924.
[28] D. J. Israel et al., "LunaNet: A flexible and extensible lunar exploration communications and navigation infrastructure," in *Proc. IEEE Aerosp. Conf.*, Mar. 2020, pp. 1–14, doi: 10.1109/AERO47225.2020.9172509.
[29] C. Capone. (Apr. 2022). *Shackleton Crater's Illuminated Rim Shadowed Interior*. [Online]. Available: https://science.nasa.gov/resource/shackleton-craters-illuminated-rim-shadowed-interior/
[30] Y. Gao, M. Abdel-Salam, K. Chen, and A. Wojciechowski, "Point real-time kinematic positioning," in *Int. Association Geodesy Symposia*, 2003, pp. 77–82.
[31] Q. T. Hoang, T. N. Le, and Y. Shin, "An RSS-comparison based localization in wireless sensor networks," in *Proc. 8th Workshop Positioning, Navigat. Commun.*, Apr. 2011, pp. 116–121, doi: 10.1109/WPNC.2011.5961026.

R. JANGALE (Graduate Student Member, IEEE) received a bachelor's degree in mechanical engineering from Texas A&M University, College Station, TX, USA, in 2023, where he is currently pursuing a Ph.D. degree in mechanical engineering with the Robotics and Automation Design (RAD) Laboratory.

He worked on the RoboBall Project since its inception with the RAD Laboratory, Bryan, TX, USA, in 2022. He worked on the early design and assembly of RoboBall II until 2023 and has since worked on the design of the RoboBall III pendulum and shell, along with the creation of supplementary robots for the robot's payload. He currently works at the RAD Laboratory. His research interests involve the design of novel robots for robust terrain mobility and terrestrial/extraterrestrial exploration.

D. PRAVECEK (Graduate Student Member, IEEE) received the B.S. degree in mechanical engineering with a minor in electrical engineering from Texas A&M University, College Station, TX, USA, in 2024, where he is currently pursuing a Ph.D. degree with the Robotics and Automation Design (RAD) Laboratory.

His research focuses on formulating and analyzing the dynamics of RoboBall II and RoboBall III, as well as designing and implementing control algorithms to enhance their ability to move faster, traverse complex terrain, and operate with greater autonomy, ultimately expanding their practical applications.

S. LAM received a bachelor's degree in mechanical engineering from Massachusetts Institute of Technology, Cambridge, MA, USA, in 2022. She is currently pursuing a Ph.D. degree in mechanical engineering with the Robotics and Automation Design (RAD) Laboratory, Texas A&M University, College Station, TX, USA.

She is currently as a Graduate Researcher with the RAD Laboratory, Bryan, TX, USA. She is also the lead of the design in RAD exploration vehicle (REV) and plans to continue with the control development for the rover in the near future.

D. MCDOUGALL received a bachelor's degree in mechanical engineering from Texas A&M University, College Station, TX, USA, in 2024, where he is currently pursuing a Ph.D. degree in mechanical engineering with the Robotics and Automation Design (RAD) Laboratory.

He has worked on the RoboBall Project since its inception at the RAD Laboratory, in 2022, as an Undergraduate Researcher. He currently works with the RAD Laboratory. He focused on the shell design and validation testing during this time. His research interests involve robotic manipulation and interaction with the environment.

M. TREVIÑO IV is currently pursuing a bachelor's degree in mechanical engineering with Texas A&M University, College Station, TX, USA.

He began working with the Robotics, Automation, and Design (RAD) Laboratory, in May 2024, as a Researcher, focusing on field robotics for planetary exploration. He will pursue the Master of Science degree in space studies with Rice University, Houston, TX, USA, where he aims to further explore the development and application of space exploration technologies. His research interests include space systems engineering, autonomous robotics, and mechanical design for extreme environments.

A. VILLANUEVA (Member, IEEE) received a bachelor's degree in mechanical engineering from University of California, Irvine, Irvine, CA, USA, in 2022.

He is a Research Engineer II with the Robotics and Automation Design (RAD) Laboratory, Texas A&M University, College Station, TX, USA. He has been working on the RoboBall Project with the RAD Laboratory since June 2024. He has worked on system integration, test engineering, manufacturing, and navigation for the project.

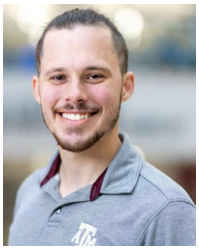

J. LAND received a bachelor's degree in computer science with a minor in cybersecurity from Texas A&M University, College Station, TX, USA, in 2024.

He currently works as a Research Engineer with the RAD Laboratory, Bryan, TX, USA, where he has been working on the RoboBall Project since May 2024. He has worked on the control code and software workflow for the project. His work has focused on building up and refining the software stack for the team.

H. DE LEON received a bachelor's degree in mechanical engineering from Columbia University, New York, NY, USA, in 2024.

Throughout her bachelor's studies, she worked as a Mechanical Design Intern with the NASA JSC's ER4 Division, where she led the chassis design of the Lunar Terrain Vehicle Ground Test Unit (LTV GTU). She currently works as a Research Engineer with the Robotics and Automation Design (RAD) Laboratory, Texas A&M University, College Station, TX, USA. Since starting at the RAD Laboratory, Bryan, TX, USA, in June 2024, she has been leading the mechanical design of the REV Chassis and has contributed to additional projects in the laboratory. She is currently working on generation 2 of the REV Rover.

M. OEVERMANN (Member, IEEE) received the B.S. degree in mechanical engineering from Texas A&M University, College Station, TX, USA, in 2021, where he is currently pursuing a Ph.D. degree with the Robotics Automation Design Laboratory, under the supervision of Dr. Robert Ambrose.

He has previously completed a student co-op with BakerRisk in 2020, supporting their blast testing and safety division. His current research focuses on developing accurate dynamic models for RoboBall. His research is extending to various other systems at the RAD Laboratory, Bryan, TX, USA.

R. AMBROSE (Member, IEEE) received the B.S. and M.S. degrees from Washington University in St. Louis, St. Louis, MO, USA, and a Ph.D. degree in mechanical engineering from The University of Texas at Austin (UT Austin), Austin, TX, USA.

He has worked as a Researcher in academia with UT Austin; as an Engineer with an FFRDC, MITRE, McLean, VA, USA and as a Project Leader with Metrica Inc., San Antonio, TX, USA, a small start-up company, followed by over 20 years in government. With the NASA's Johnson Space Center from 2000 to 2021, he was as the Project Manager, the Branch Chief, and later as the Division Chief of the Software, Robotics, and Simulation Division. He retired from NASA in 2021 and accepted the Endowed Chair at Texas A&M University, College Station, TX, USA, as the J. Mike Walker "66 Chair in mechanical engineering, with courtesy appointments at the Department of Aerospace Engineering and the Department of Electrical Engineering. He serves as the Associate Director of Texas A&M Space Institute, the Director for Space and Robotics Initiatives of Texas Engineering Experiment Station, and the Associate Director of space and robotics research at the Bush Combat Development complex on Texas A&M's RELLIS Campus.